Dynamics of Atmospheres and Oceans, 11 (1987) 175–201
Elsevier Science Publishers B.V., Amsterdam – Printed in The Netherlands

WIND-DRIVEN OCEAN CIRCULATION TRANSITION TO BAROTROPIC INSTABILITY

CHRISTIAN LE PROVOST and JACQUES VERRON

Institut de Mécanique de Grenoble, BP 68, 38402 St. Martin D'Heres Cedex (France)

(Received March 24, 1986; revised March 9, 1987; accepted March 30, 1987)

ABSTRACT

Le Provost, C. and Verron, J., 1987. Wind-driven ocean circulation transition to barotropic instability. Dyn. Atmos. Oceans, 11: 175–201.

This article deals with the ocean circulation driven by steady zonal winds, and damped by bottom and biharmonic friction, when represented by the simple barotropic vorticity equation. A double gyre antisymmetrical wind stress pattern in a square basin is considered. Wind forcing and dissipation parameters are chosen within the ranges of what has been used in previous studies. The flow characteristics for both steady and unsteady situations are tentatively described as functions of model external parameters through the analysis of a large set of numerical experiments. Functional relations are derived for the mid-latitude jet parameters (length, width and transport) on the basis of scaling arguments. With the diagrams established for these quantities in forcing and dissipation parameter space, these relations allow quantitative predictions of model response to a wide range of parameter choices to be made. The transition to barotropic instability is interpreted by analysing and comparing the spin-up phase of different numerical experiments leading either to stable or unstable solutions. Two major types of destabilization are identified, namely through meandering of the mid-latitude eastward jet and Rossby wave radiation from the westward return flow. The characteristics of the flows are shown to be highly sensitive to the external parameter changes. Competition between eddy kinetic energy level and eastward jet extension appears to constitute the key point of this class of solutions, controlling in particular the intensity of transport in the inner gyres, driven by the eddy field on the two sides of the mid-basin jet, in a very similar manner to that of the more complex multilayered EGCMs.

1. INTRODUCTION

A review of the literature concerning the solutions of the barotropic vorticity equation, in the context of general ocean circulation driven by steady zonal winds, shows that relatively little has been written in this domain since Bryan (1963), Veronis (1966a,b) and Blandford (1971). These authors used numerical investigations to extend to highly non-linear situa-

0377-0265/87/$03.50

tions the analytical results obtained, following the pioneering work of Sverdrup (1947), Stommel (1948) and Munk (1950), by a large number of authors including Charney (1955), Morgan (1956), Carrier and Robinson (1962), Moore (1963), Stewart (1964), Veronis (1964), Niiler (1966), Holland (1967) to mention but a few. Indeed, attention quickly focussed on the baroclinic General Circulation Models (GCMs) and the multilayer Eddy Resolving General Circulation Models (EGCMs). New insights have been obtained from these more complex models in terms of our understanding of the interactions occurring in mid-latitude ocean basins, which stand in contrast to the classical steady or quasi-steady wind driven circulation theories previously cited.

However, given the difficulties in analysing the physics of these EGCM results under different model physical assumptions and parameter ranges, several authors have recently reconsidered the simpler barotropic wind driven problem, and analysed the energy budgets and vorticity balances over regions of the wind driven gyres: Harrison and Stalos (1982) have taken a fresh look at the Veronis (1966) non-linear calculations with bottom friction damping; Marshall (1984) has shown how the barotropic instability of a jet, separating counter-rotating gyres, transfers from one gyre to the other the vorticity required to maintain a statistically steady state. Böning (1986) has investigated the case where lateral viscosity is the dominant factor of dissipation. The present work is of the same ilk, but focusses on the two gyre problem, steady and unsteady, over a range of parameters corresponding to realistic basin sizes and wind forcing, and low dissipation rates.

The aim of this study is to investigate the barotropic response of a square ocean driven by a steady double gyre antisymmetrical wind pattern, using a large set of numerical experiments. Attention is focussed on some major characteristics of the flows such as the eastward extension, width and transport of the mid-latitude jet, and their dependence on the controlling parameters, forcing and dissipation. Of particular interest is the transition from stable to barotropically unstable solutions.

Although the experiments reported are all barotropic, they are very convenient for analysis and rationalization, and this can be usefully applied to the understanding of the upper layer dynamics of multi-layered QG models, by allowing the study of the barotropic instability properties of the flows and the vorticity transfer mechanisms from one gyre to the other independently of the baroclinicity. Section 2 provides a brief review of the model formulation and controlling parameters, and the characteristics of the numerical model used. In section 3, the controlling parameter space, which may be considered as relevant to the ocean, is quantitatively specified. The set of steady solutions is presented and analysed in section 4, with a rationalization of the jet extension and transport. Transition to barotropic instability is clarified in section 5 through examination of the spin-up in several experiments which led either to steady or unsteady solutions. The essential features of the unstable solutions are then briefly presented, and the role of lateral friction on these flows is illustrated in section 6.

2. FORMULATION

The classical, fundamental, barotropic vorticity equation (BVE), derived for a wind-driven ocean in a closed basin of constant depth D, is

$$\partial/\partial t(\zeta) + J(\psi,\zeta) + \beta_0 \cdot \partial\psi/\partial x = 1/D \cdot \mathrm{curl}\ \tau + Dv + Df \quad (1)$$

where ζ is the vorticity and ψ the streamfunction. The vertically averaged velocity components $(u,\ v)$ are given by $u = -\partial\psi/\partial y$ and $v = \partial\psi/\partial x$. Circulations are induced by the surface wind stress, τ, and controlled by lateral (Dv) and bottom (Df) dissipation processes. By considering an Ekman bottom layer, Df can be expressed as a simple linear form

$$Df = -K\zeta \quad (2)$$

where $\tau a = 1/K$ is the bottom friction damping timescale. For lateral friction, the constant eddy viscosity hypothesis leads to the Laplacian formulation

$$Dv_1 = A\Delta\zeta \quad (3)$$

which was used in early work (Munk, 1950; Bryan, 1963). However, results from EGCM investigations have shown the value of higher order viscosity which is more selective in terms of modelling the dissipation of enstrophy at higher wave numbers (Charney, 1971; Holland, 1978). The biharmonic formulation is thus commonly used in EGCM studies

$$Dv_2 = -A_4\nabla^4\zeta \quad (4)$$

It is convenient to discuss the problem in non-dimensional terms. In the following section, the basin geometry is a square box of typical size L, and the wind field, a simplified two gyre antisymmetrical pattern

$$\begin{cases} \tau_x = -\tau_0/\rho \cdot \cos(2\pi y/L) \\ \tau_y = 0 \end{cases} \quad (5)$$

A typical scale for the velocity is given by the Sverdrup balance

$$U = 2\pi\tau_0/\rho D\beta_0 L \quad (6)$$

A characteristic timescale is $T = (\beta_0 L)^{-1}$, and can be related to the timescale of the fastest barotropic Rossby wave crossing the basin.

The classical non-dimensional numbers are introduced

$R = 2\pi\tau_0/\rho D\beta_0{}^2 L^3$	Rossby number
$Ef = K/\beta_0 L$	Vertical Ekman number
$Ev_1 = A/\beta_0 L^3$	Horizontal Ekman number
$Ev_2 = A_4/\beta_0 L^5$	Biharmonic Ekman number

The non-dimensional form for eq. 1 is then

$$\partial/\partial t'(\zeta') + R \cdot J(\psi', \zeta') + \partial/\partial x'(\psi')$$
$$= -\sin 2\pi y' + Ev_1 \nabla^4 \psi' - Ev_2 \nabla^6 \psi' + Ef \nabla^2 \psi' \tag{7}$$

From these numbers, the following parameters can be derived

$$\delta i = R^{1/2},\ \delta f = Ef,\ \delta v_1 = Ev_1^{1/3},\ \delta v_2 = Ev_2^{1/5}$$

They characterize the western boundary layer scales. A characteristic width of the western boundary current may be associated with each dominant process

$$\begin{aligned} &\text{inertial effect (Fofonoff, 1954): } Wi = \delta i \cdot L \\ &\text{bottom friction (Stommel, 1948): } Wf = \delta f \cdot L \\ &\text{lateral friction (Munk, 1950): } Wv_1 = \delta v_1 \cdot L \\ &\text{biharmonic friction (Holland, 1978): } Wv_2 = \delta v_2 \cdot L \end{aligned} \tag{8}$$

The boundary conditions play a critical role in model solutions. For single gyre cases Blandford (1971) has shown how the same set of parameters may lead either to steady flows, with western and northern boundary currents, or to unsteady flows, with a western boundary current and eddies in the northwest corner, depending on whether a slip or no-slip condition is applied along the boundaries. The physical relevance of such conditions is questionable, although most of the recent EGCM have used slip conditions. The question was addressed recently, for example, by Marshall (1984) when he introduced an unconventional boundary condition on the vorticity gradient ensuring no net dissipation of vorticity along the walls. As we want to contribute here to rationalize classical EGCM results, we follow usual EGCM practice and take as boundary conditions in the following

$$\psi = 0,\ \partial^2/\partial n^2(\psi) = 0,\ \partial^4/\partial n^4(\psi) = 0 \tag{9}$$

Equation 7 is integrated numerically using a standard finite difference model. Second order difference approximations are used for both space and time derivatives: the vorticity equation is leap-frogged forward in time, the jacobian is represented by central differences in time and Arakawa's (1966) formulation in space. Bottom friction is evaluated through a semi-implicit scheme, averaging the values at the preceding and succeeding time levels. Laplacian terms are calculated by following a classical five point procedure. The finite difference version of the Poisson equation, enabling ψ to be computed from ζ at each time step, is solved by a FFT method involving cyclic reduction. In every case the grid scale is chosen in such a way as to resolve the western inertial boundary current (WBC) and the mid-latitude jet (at least 3 points in the WBC, which is a minimum, knowing that the results can be very sensitive to resolution).

3. PARAMETER RANGE UNDER INVESTIGATION

When addressing the problem of the Gulf Stream system, and the mid-latitude wind-driven circulations at the scale of the North Atlantic, we have to consider horizontal scales of the order of several thousand kilometers; in general, we used a square basin 2000 km or 4000 km in width. Depending on the way the problem was considered, depth was either 1000 m, corresponding to the dynamics of the upper ocean, or 5000 m for total barotropic flow. In so far as vorticity transfer is concerned, Harrison (1982) has argued that the upper layer dynamics, as predicted from the most recent multilayer EGCM experiments, are the same as for the BVE with domain depth equal to the previously mentioned upper layer depth almost everywhere. As pointed out earlier, the study of the BVE is thus of particular relevance to gaining an understanding of the upper layer dynamics in these more complex experiments.

Over the North Atlantic, the mean wind stress is of the order of 1 dyne cm^{-2} (i.e. 0.1 N m^{-2}) and can vary by as much as 5 dynes cm^{-2} over a month. Consequently, if the planetary vorticity gradient is taken to be $\beta_0 = 2 \cdot 10^{-11}$ m^{-1} s^{-1}, a typical δi range is from $0.5 \cdot 10^{-2}$ ($\tau_0 = 0.1$ N m^{-2} assuming $L = 4000$ km, $D = 1000$ m) to $3.13 \cdot 10^{-2}$ ($\tau_0 = 0.5$ N m^{-2} assuming $L = 2000$ km, $D = 1000$ m) (see Fig. 1).

It is more difficult to define the range of parameters relevant to the ocean for δf and δv because the frictional parameterizations are not, as yet, fully justified. Although subject to uncertainties, the oceanic values for $\tau a = 1/K$ must surely be of the order or higher than 100 days. In Fig. 1, where the correspondence between δf and the bottom friction timescale, τa, is given for different basin sizes, the oceanic flows appear to be strongly inertially controlled for realistic range of forcing parameters.

The lateral friction timescale has to be characterised differently because it depends on the scale of motion under consideration. Figure 2 shows such timescales for three different values of each possible parameterization (Laplacian and biharmonic). In both cases, the damping timescales for the largest scales of motion are very large. The dynamics of these largest scales

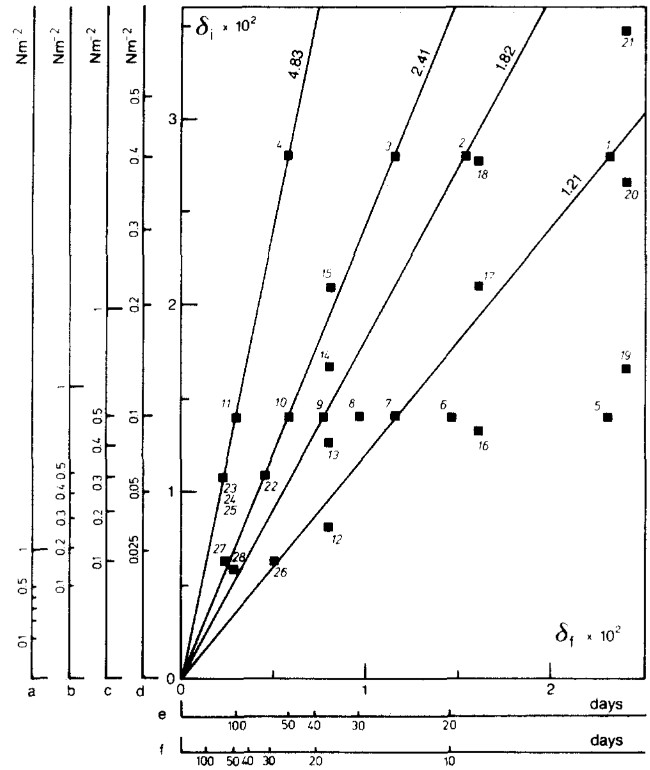

Fig. 1. Location of the complete set of experiments in the (δi, δf) parameter space, and scaling relations between δi, δf and the physical quantities τ_0 and τa for various (L, D) domains. (a) $L \times L = 4000$ km$\times$4000 km, $D = 5000$ m. (b) $L \times L = 4000$ km$\times$4000 km, $D = 1000$ m. (c) $L \times L = 2000$ km$\times$2000 km, $D = 5000$ m. (d) $L \times L = 2000$ km$\times$2000 km, $D = 1000$ m. (e) $L \times L = 2000$ km$\times$2000 km. (f) $L \times L = 4000$ km$\times$4000 km.

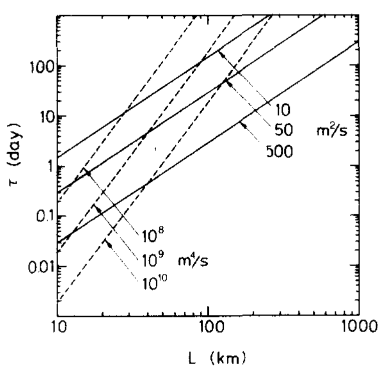

Fig. 2. Characteristic lateral friction timescale versus wavelength for several values of A_4 (m^4 s^{-1}) or A coefficient (m^2 s^{-1}).

may therefore be taken to be quasi-inviscid. Consequently, under steady flow regimes the parameter δv_1 (or δv_2) will presumably not control the general circulation to any great extent (in a context of slip boundary conditions). However, this will no longer hold true for the unsteady cases because the flow instabilities will now develop eddies at the mesoscale which can be strongly affected by the dissipation process at the gridscale, where the enstrophy cascade modelling may be critical. Thus, we can expect the parameters δv_1 and δv_2 to influence the general (mean and eddying) circulation in such unsteady situations, in contrast with the steady flow cases.

4. RANGE OF PARAMETERS LEADING TO STEADY FLOWS

Veronis (1966a,b) has studied the single gyre problem intensively, and Harrison and Stalos (1982) have recently reconsidered this problem and presented some double gyre cases. In the limit of very weak (linear) flows ($R \rightarrow 0$), the solution is similar to the Stommel (1948) solution. When inertial effects are increased, or damping is decreased (i.e. the ratio $\delta i/\delta f$ goes up), the solution changes greatly as non-linear effects become more important. Let us look in greater detail at the antisymmetrical double gyre case, which differs from the single one by the presence of a mid-basin free jet instead of a northern boundary layer.

A large number of experiments were carried out within the parameter range given in Table I. The distribution of these experiments in the (δi, δf) parameter space is shown in Fig. 1. All the experiments started from an initial state of rest, and computations were performed until steady circulation was reached. The duration of the integration generally needed to be around three times the bottom friction timescale.

Some typical steady flow patterns are presented in Figs. 3 and 4. This set of experiments illustrates to some extent the similarity between the well-known one-gyre case and the two-gyre case under investigation here. As the damping coefficient is reduced, the solution evolves from a quasi-linear Stommel-type solution (Fig. 3-1) to strongly non-linear inertially-dominated flows (Fig. 3-9). In Fig. 3-1, the Sverdrup dynamics regime dominates most of the basin. The slight asymmetry within each gyre is due to a weak boundary current advection, towards the zero wind stress curl latitude, of excess negative (positive) relative vorticity which is not damped rapidly enough within the WBC flowing northward (southward). The particles moving northward or southward along this side have exactly the same magnitude of vorticity in the southern and northern gyre. Consequently their vorticities cancel out, when they meet one another along the zero wind curl line. The other particles retain their vorticity when leaving the vicinity of the

TABLE I

External parameters of the experiments discussed in this study

Experiment	$\tau_0 \times 10^{-1}$ Nm^{-2}	$K \times 10^{-1}$ s^{-1}	$A_4 \times 10^9$ $m^4\ s^{-1}$	$\delta i \times 10^{-2}$	$\delta f \times 10^{-2}$
1	20	9.24	8	2.8	2.31
2	20	6.16	1	2.8	1.54
3	20	4.64	8	2.8	1.16
4 unst.	20	2.32	8	2.8	0.58
5	5	9.24	1	1.4	2.31
6	5	5.8	1	1.4	1.45
7	5	4.64	1	1.4	1.16
8	5	3.84	1	1.4	0.96
9	5	3.08	1	1.4	0.77
10	5	2.32	1	1.4	0.58
11 unst.	5	1.2	1	1.4	0.30
12	1.6	3.2	1	0.8	0.8
13	4.04	3.2	1	1.26	0.8
14	7.1	3.2	1	1.67	0.8
15	11.34	3.2	1	2.11	0.8
16	4.5	6.4	1	1.33	1.6
17	11.34	6.4	1	2.11	1.6
18	19.53	6.4	1	2.11	1.6
19	7.02	9.6	1	2.77	1.6
20	17.88	9.6	1	1.66	2.4
21	30.84	9.6	1	2.65	2.4
22	3	1.8	1	3.48	2.4
23 unst.	3	0.8	0.1	1.09	0.23
24 unst.	3	0.8	1	1.09	0.23
25 unst.	3	0.8	10	1.09	0.23
26	1	2	0.1	0.63	0.50
27 unst.	1	0.8	0.05	0.63	0.23
28 unst.	0.9	1	0.05	0.59	0.27
29	20	20	8	2.8	5

coast. This explains why they undergo a southward (northward) displacement before joining the Sverdrup flow. As the damping is decreased, the inertia of the flow is augmented, leading to the formation of a zonal mid-basin jet, penetrating eastward. Simultaneously, the excess of vorticity carried by the jet produces return flows which are clearly visualized in Fig. 3-7, -8, -9. Moving southward (northward), these particles lose their negative (positive) relative vorticity. Their inertia makes them overshoot the zero vorticity position and acquire some positive (negative) vorticity by going too far south (north). This vorticity gain (see Fig. 4) leads to a tight eastward return of the particles which finally end up in the Sverdrup flow. These

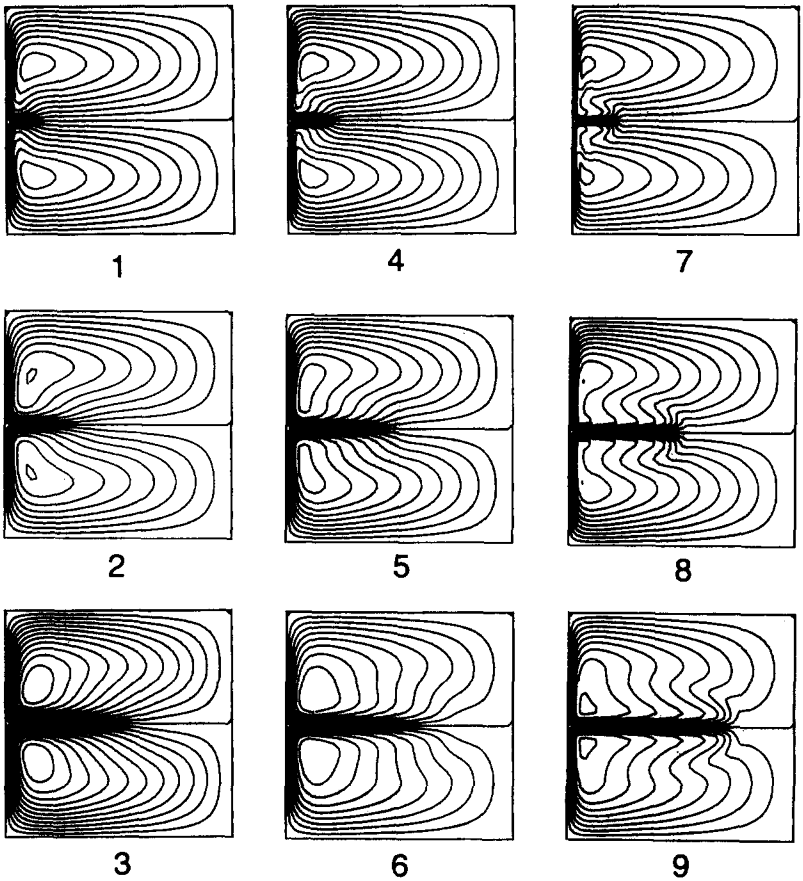

Fig. 3. Streamfunction pattern for some steady flows and different (δi, δf) values: 1- experiment 19 (1.65, 2.4), 2- experiment 20 (2.65, 2.4), 3- experiment 21 (3.48, 2.4), 4- experiment 16 (1.33, 1.6), 5- experiment 17 (2.11, 1.6), 6- experiment 18 (2.77, 1.6), 7- experiment 12 (0.80, 0.8), 8- experiment 13 (1.26, 0.8), 9- experiment 14 (1.67, 0.8).

characteristics are much more pronounced when bottom damping is weaker. Moreover, in the limit of very weak bottom damping, the jet reaches the eastern wall and the solution tends to take on a Fofonoff-like pattern. Note, however, that Harrison and Stalos (1982) have shown that it is not a Fofonoff balance.

The penetration length of the jet is also related to inertial effects: for a given bottom friction coefficient, this length increases with δi. In fact, the jet seems to be of approximately the same extent when δi and δf vary simultaneously within the same ratio (Fig. 5). Furthermore, the width of the WBC and the jet become thinner when δi is decreased, according to the non-linear western boundary layer theory (Pedlosky, 1979).

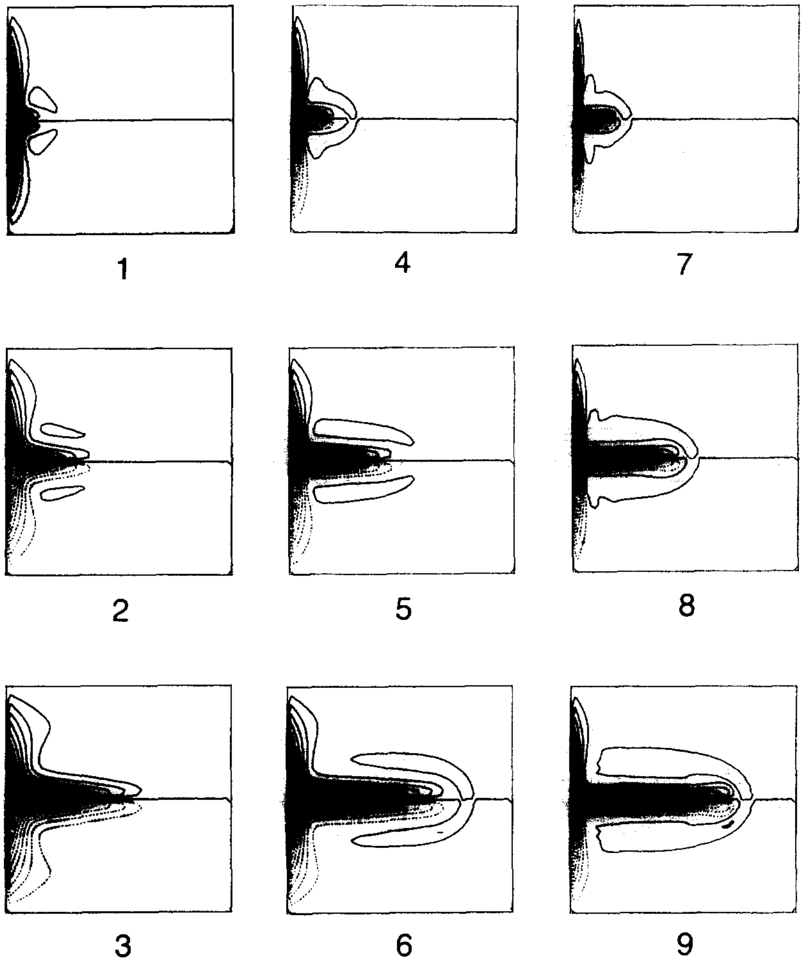

Fig. 4. Vorticity patterns under the same conditions as in Fig. 3.

To understand the relationship between the different processes going on when varying the forcing (δi) and damping (δf) parameters, let us specify some jet dynamical quantities for which values can be determined from the numerical solutions:

(1) the maximum transport in each gyre, quantified as $T = \psi_{max} D$ given the fact that ψ is taken to be zero along the basin walls;

(2) the eastward jet extension, Lj, measured from the zero line in the vorticity field (Fig. 4);

(3) the transport Tj in the half jet, which is assumed to be the transport through each gyre: this assumption is valid for most of the stable cases; and

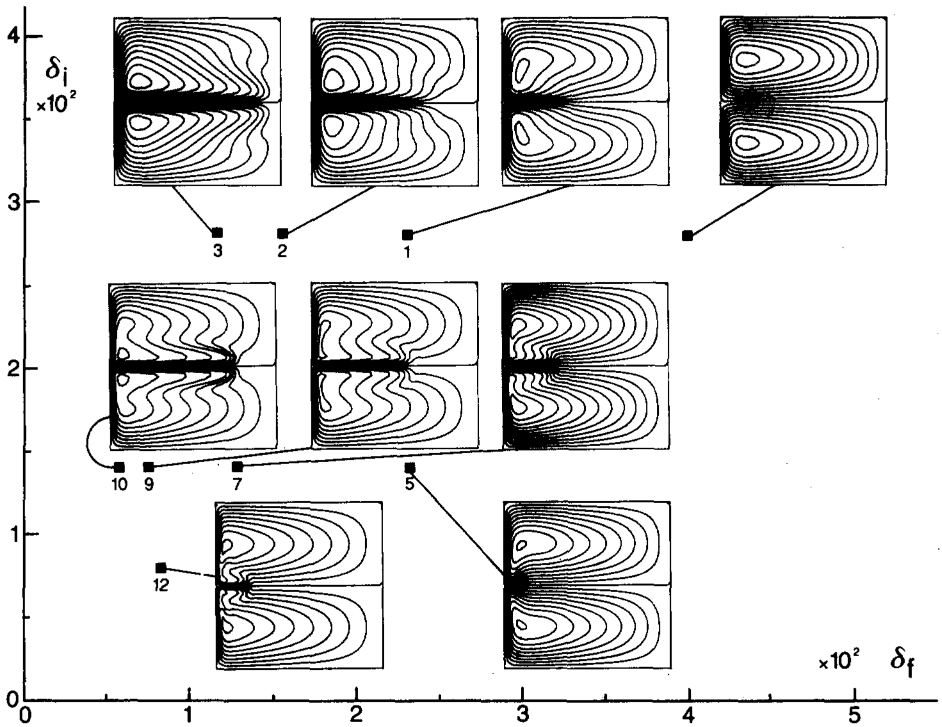

Fig. 5. Typical steady flow streamfunction patterns in the $(\delta i,\ \delta f)$ parameter space.

(4) Uj and Vj, the zonal and meridional velocities in the main part of the jet, and λj, the half jet width.

The set of experiments listed in Table I enabled us to investigate the dependence of the quantities Lj/L and T/Ts on the external parameters δi and δf in Figs. 6 and 7 (Ts is the Sverdrup transport defined as $Ts = 2\pi\tau_0/\rho\beta_0$). This dependence is quite complex. The eastward jet extension is not strictly related to $\delta i/\delta f$, as qualitatively noticed before; and the maximum transport in the basin is strongly dependent on δi and δf: the T/Ts transport relationship reaches a minimum before increasing up to nearly 1 when wind forcing is increased while bottom friction damping timescale is held constant. This has already been pointed out by Véronis (1966), and the present set of experiments confirms the existence of this counter intuitive result.

In line with the work done by Harrison and Stalos (1982) in terms of single gyre dynamics, it is possible to establish some degree of functional dependency between the jet flow characteristics and the model parameters. Near the mid-latitude of the basin, along the axis of the jet, the wind stress

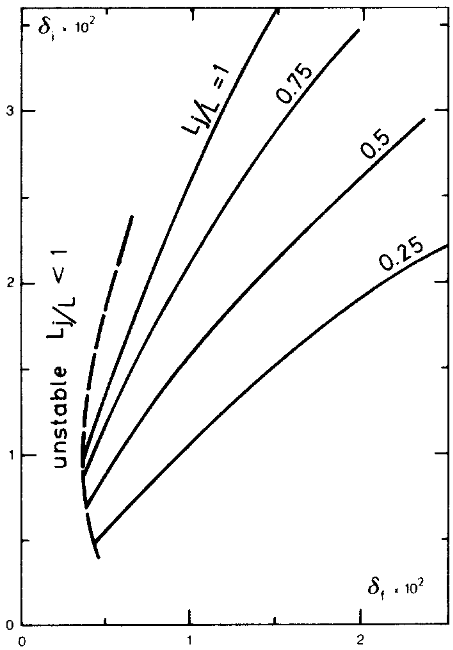

Fig. 6. Isolines of relative jet length Lj/L in the $(\delta i,\ \delta f)$ parameter space.

curl contribution is small and may be neglected in the local jet dynamics. Thus, eq. 1 reduces, under the stationary regime, to

$$u\partial\zeta/\partial x + v\delta\zeta/\partial y + \beta v = -K\zeta \tag{13}$$

Equation 13 can be made dimensionless relative to the jet scales

$$u' = u/Uj;\ \ y' = v/Vj;\ \ x' = x/Lj;\ \ y' = y/\lambda j;\ \ \zeta' = \zeta'/\Omega j$$

A characteristic vorticity in the jet is denoted Ωj. Thus we obtain

$$u'\partial\zeta'/\partial x' + v'\partial\zeta'/\partial y' \cdot (VjLj/Uj\lambda j) + v' \cdot (\beta VjLj/Uj\Omega j)$$
$$= -\zeta' \cdot (KLj/Uj) \tag{14}$$

Two cases may be considered here.

(1) If we assume a balance between the different terms that are involved in the previous equation, i.e. inertia, bottom friction and β-effect are all playing an O(1) role, we obtain the following relationships for the velocity components and the vorticity

$$Uj \sim KLj \qquad Vj \sim K\lambda j \qquad \Omega j \sim \beta_0 \lambda j$$

A way of determining a vorticity scale in the jet is to assume that the bulk of the vorticity loss occurs in the jet, i.e. the vorticity dissipation within each

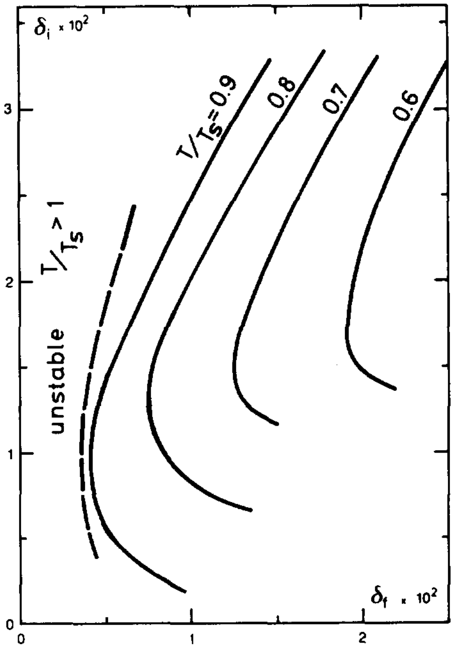

Fig. 7. Isolines of maximum transport (T/Ts) in the basin in the (δi, δf) parameter space.

half-jet is of the order of the vorticity input from the wind over each half-basin

$$\int_{\substack{\text{half}\\ \text{jet}}} K\zeta \, \mathrm{d}x \, \mathrm{d}y \sim \int_{\substack{\text{half}\\ \text{basin}}} 1/D \cdot \operatorname{curl} \tau \, \mathrm{d}x \, \mathrm{d}y$$

i.e.

$$K\Omega j Lj \lambda j \sim \tau_0 L/\rho D$$

This gives a scaling for the vorticity of

$$\Omega j \sim \tau_0 L/\rho K D Lj \lambda j$$

The transport, Tj, can then be deduced as

$$Tj \sim Uj\lambda j D \sim Ts\ \delta f^{1/2}(Lj/L)^{1/2}\ \delta i^{-1}$$

The relative jet length can then be written as

$$Lj/L \sim (Tj/Ts)^2(\delta i/\delta f)\delta i \tag{15}$$

(2) If we consider the highly non-linear domain where the jet is strongly dominated by its zonal inertia, the vorticity can be scaled as

$$\Omega j \sim Uj/\lambda j$$

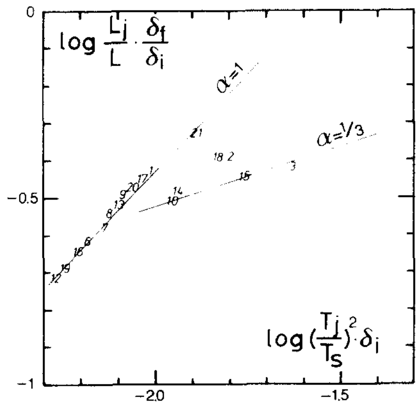

Fig. 8. Functional relationship between Lj/L, T/Ts, δi and δf. Experimental verification of relationship (17) and of the existence of two regimes: moderately non-linear ($\alpha = 1$) and strongly non-linear ($\alpha = 1/3$), over the domain of non-linear stable solutions.

The main equilibrium is thus within zonal advection of vorticity and its dissipation, on the one hand, and meridional advection of vorticity and β-effect, on the other

$$Uj \sim KLj \qquad \Omega j \sim \beta_0 \lambda j$$

The transport, Tj, consequently takes the form

$$Tj \sim Ts(Lj/L)^{3/2}(\delta f/\delta i)^{3/2}\delta i^{-1/2}$$

while the relative jet length becomes

$$Lj/L \sim (Tj/Ts)^{2/3}\delta i/\delta f\ \delta i^{1/3} \tag{16}$$

and the half jet width $\lambda j/L = R^{1/3}$

From (15) and (16), the jet extension can be written under the general relationship

$$Lj/L \sim \delta i/\delta f\left[(Tj/Ts)^2\delta i\right]^{\alpha} \tag{17}$$

With $\alpha = 1$ for a broad range of parameters where inertia and damping are of the same order, and $\alpha = 1/3$ in the case of highly inertial regimes. In Fig. 8, the relationships between $Lj/L \cdot \delta f/\delta i$ and $(Tj/Ts)^2\delta i$ are shown logarithmically for the set of experiments leading to steady solutions. Clearly, most of the data set is consistent with the preceding relations: eq. 15 is satisfied up to $Lj/L \sim 0.7$, and eq. 16 for $Lj/L > 0.75$, except in the case of very weak forcing. In these latter cases, part of the flow joins the Sverdrup circulation directly without first going through the mid-latitude jet (see, for example, Fig. 3.7) and then scaling assumptions are untrue.

5. RANGE OF PARAMETERS LEADING TO UNSTEADY FLOWS

In the preceding section, it was seen that, for large $\delta i/\delta f$ ratios, the appropriate scaling of the vorticity in the jet was

$$\Omega j \sim Uj/\lambda j \sim \beta_0 \lambda j$$

This implies that the zonal jet velocity scaling is

$$Uj \sim \beta_0 \lambda j^2$$

But we know that a necessary criterion for horizontal shear instability is that the absolute vorticity gradients cancel

$$\left(\beta_0 - \partial^2 Uj/\partial y^2\right) = 0 \text{ i.e. } Uj \sim \beta_0 \lambda j^2$$

Thus, the jet must reach barotropic instability conditions for large $\delta i/\delta f$ ratios.

Moreover, it was noticed earlier that the relative transport T/Ts tends to increase for very small δi. As the western boundary layer and the jet widths decrease with δi, it is also to be expected that shear instability will occur for inertial flows with small δi. To understand the way these kinds of wind driven flows go to unsteadiness, it is instructive to analyse the spin-up phase of these experiments. As stated immediately above, two cases can be distinguished.

5.1. Transition to instability when decreasing the jet width for moderately non-linear flow

Several experiments were carried out for $\delta i/\delta f = 2.5$ (experiments 3, 10, 15, 22, 27), and led to steady solutions except for the last one. Two of these are presented in Fig. 5. The final streamfunction pictures look very similar, except that jets grow narrower as wind stress and bottom friction are decreased. But these results are obtained after a spin-up phase during which the meridional velocity gradient in the jet is considerably increased locally; for very small δi this allows the development of shear instabilities which can lead to fully developed unstable flows. A sequence of successive streamfunctions for such a case (experiment 27) is displayed in Fig. 9. At the beginning of the jet formation (Fig. 9a), the excess of vorticity is so great that two strong recirculating sub-gyres are induced on each side of the jet, increasing the transport there to significantly higher values than the Sverdrup transport, and this occurred for most of the experiments. In Fig. 10 the maximum transports (normalized by Ts) have been drawn versus time (normalized by the characteristic bottom friction timescale) to illustrate how the transport in the jet is temporarily enhanced during each spin-up phase by the existence

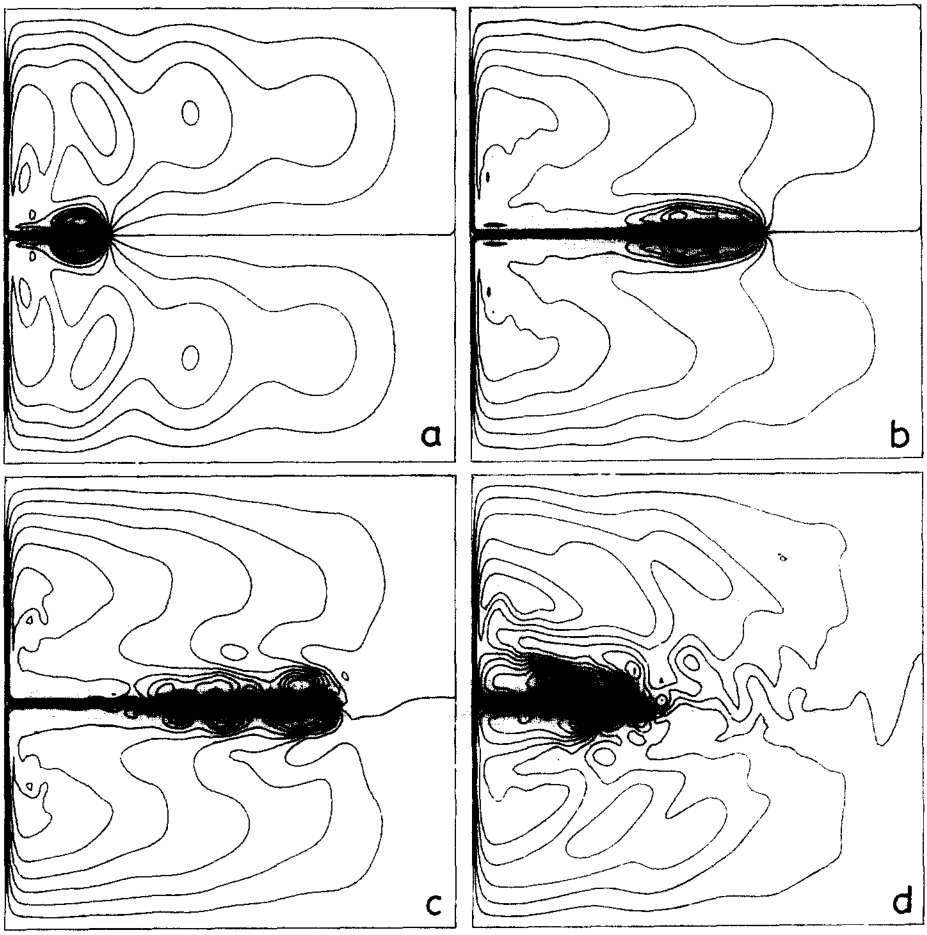

Fig. 9. Instantaneous streamfunction patterns for experiment 27: (a) $t/\tau a = 0.69$, (b) $t/\tau a = 1.72$, (c) $t/\tau a = 2.41$, (d) $t/\tau a = 3.79$. (C.I. = 0.16 Ts).

of these subgyres. As the jet increases its eastward penetration, dissipation inside the western boundary layer and inside the jet progressively gets rid of the vorticity advected from the western wall (Fig. 9b). For experiments 3, 10, 15, and 22, after a spin-up phase of about four times the damping timescale, the local subgyres disappear, and a final steady flow is obtained, with a straight and regular jet, and northwest and southwest returning flows, as already described in the previous paragraph (see Fig. 5).

But for experiment 27, as the typical width of the jet is very narrow, in close relationship with the inertial scale δi, the flow becomes unstable within the two subgyres drifting westward at the extremity of the jet. Meanders appear (see Fig 9c): on the one hand, they are advected eastward by the flow, and on the other hand, meandering propagates westward, destabilizing

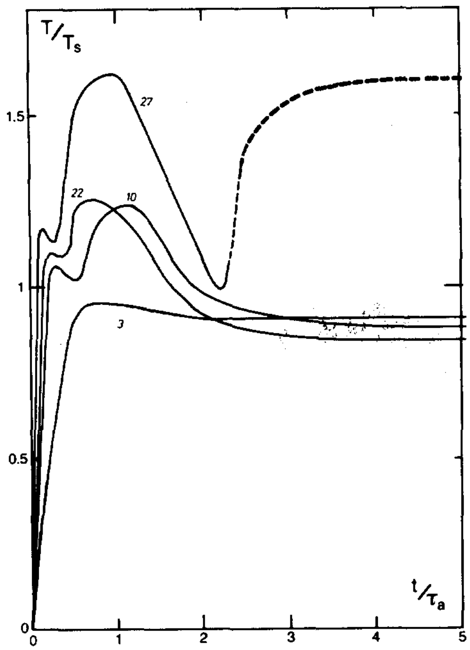

Fig. 10. Maximum transport as a function of time for a set of strongly non-linear experiments ($\delta i/\delta f \sim 2.5$). For experiment 27, the flow is fully unstable by $t/\tau a \sim 2.4$. The dashed line corresponds then to the mean transport value.

most of the jet. A part of the energy is thus transferred from the mean flow to this smaller scale variability, stopping the inertial eastward zonal penetration of the jet. This is clearly illustrated in Fig. 11a, which corresponds to the time history of the streamfunction along the latitude $y = 0.505L$, i.e. very near the axis of the jet. At $t = 2\tau a$, the jet reaches its maximum eastward extension. Its shortening occurs very abruptly. However, it takes about $2\tau a$ for the flow to adjust itself to a new equilibrium. It finally reaches a statistically steady state with a zonal penetration considerably reduced down to one quarter of the basin width, whereas the equivalent preceding steady state solutions led to jet penetration of up to $0.9L$. How does this destabilization occur? Where do instabilities first take place? It is difficult to analyse the details of this phase of destabilization on experiment 27, because it happens very abruptly. It is easier to follow these processes on experiments with broader jets and subgyres, i.e. with larger δi.

5.2. Transition to instability when increasing non linearity for strongly non linear flows

Several experiments have been carried out with a constant $\delta i(0.014)$, but decreasing δf, i.e. smaller and smaller bottom friction (experiments 5–11).

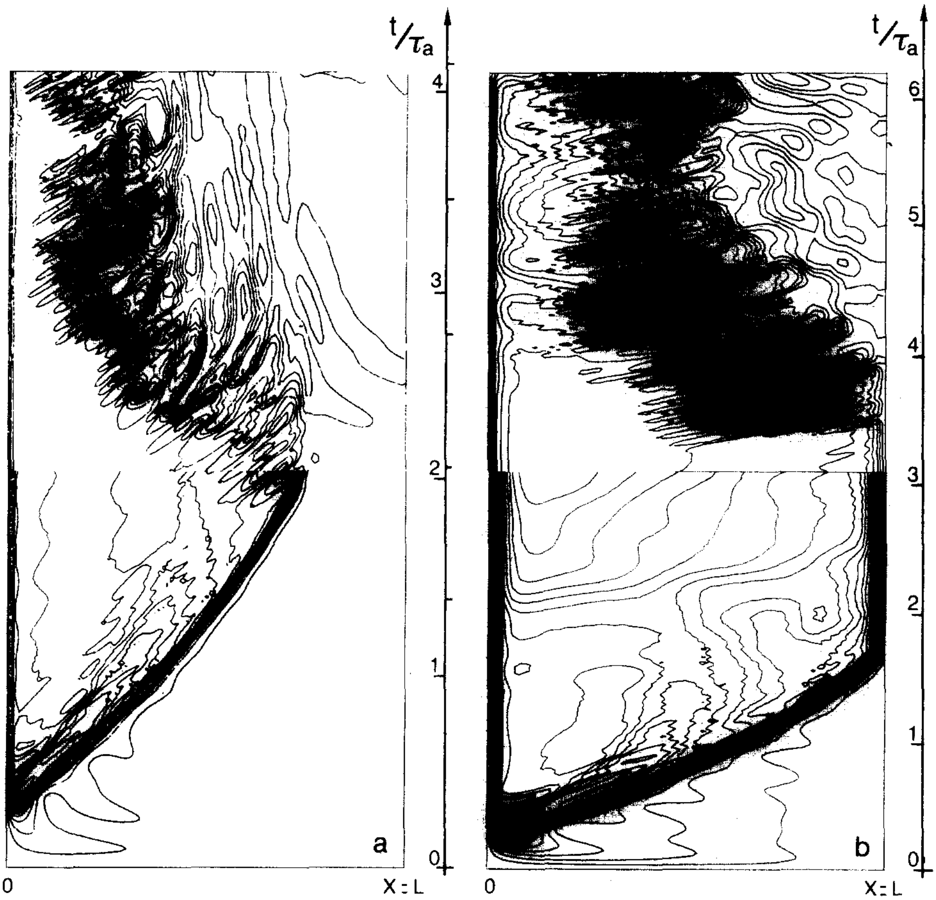

Fig. 11. Time history diagram of the stream function along the zonal section $y = 0.505L$, for: (a) experiment 27 (C.I. = 0.06 Ts for $t/\tau a < 2$, and 0.16 Ts for $t/\tau a > 2$), (b) experiment 11 (C.I. = $0.032Ts$ for $t/\tau a < 3$, and 0.13 Ts for $t/\tau a > 3$).

All of them, except experiment 11, led to steady solutions. They are displayed in Fig. 5. Let us analyse in greater detail this last experiment, in the context of a very non-linear flow ($\delta i/\delta f = 5$).

At the beginning, the basin spin-up evolves in the same way as described previously: a pair of intense recirculating subgyres develop at the extremity of the jet (Fig. 12a), penetrate eastward at the mid-latitude of the basin, and locally increase transport up to 1.7 Ts, before slowly decreasing, because of vorticity dissipation within the jet. However, as the jet is very inertial, it finally crosses the whole basin before any instabilities appear. The flow builds up an eastern boundary layer, and a strong westward recirculation; and it is in this return flow that instabilities first appear. In Fig. 12b, we

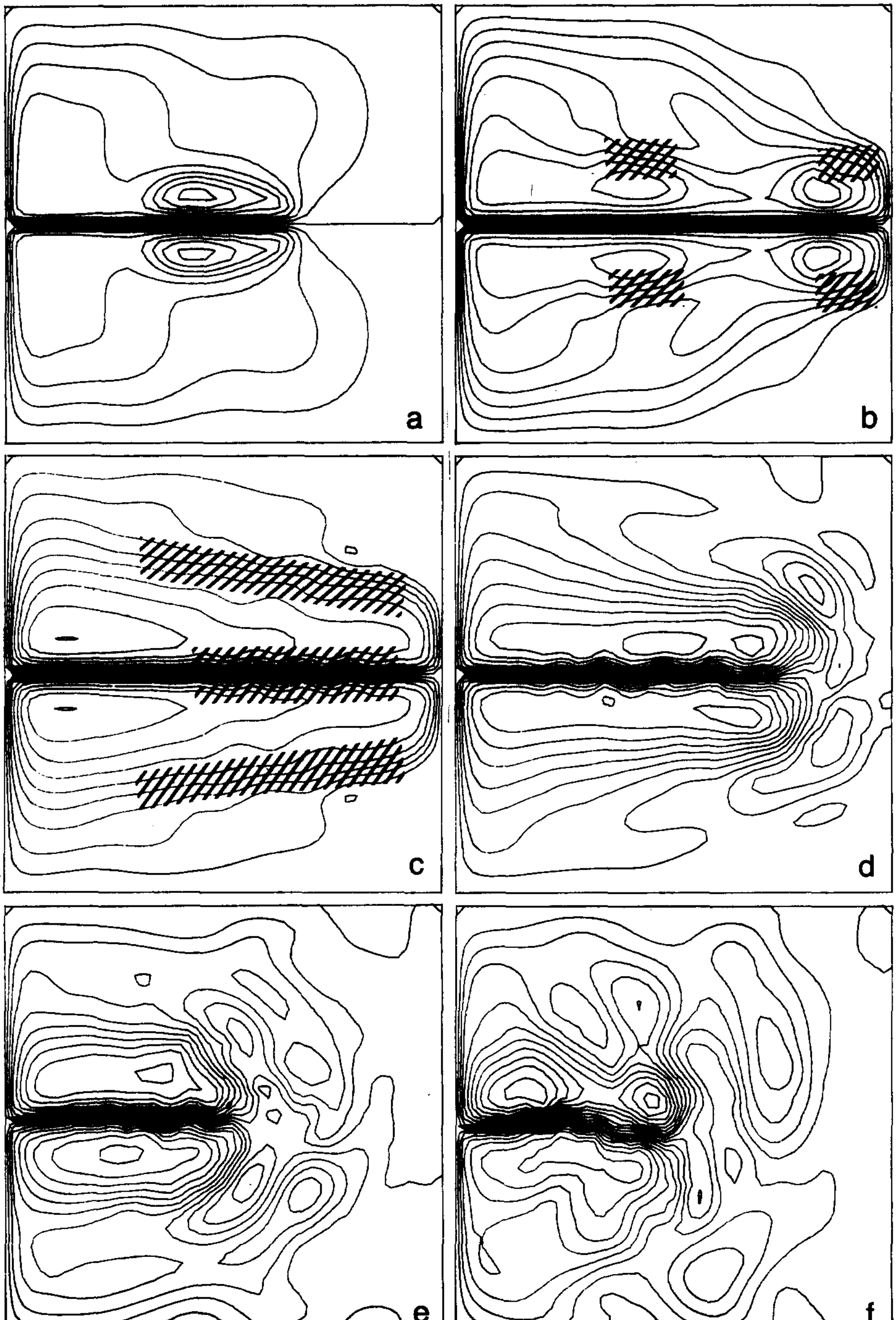

Fig. 12. Instantaneous streamfunction pattern for experiment 11: (a) $t/\tau a = 1.04$, (b) $t/\tau a = 2.1$, (c) $t/\tau a = 3.3$, (d) $t/\tau a = 4.35$, (e) $t/\tau a = 5.3$, (f) $t/\tau a = 6.24$. (C.I. = 0.19 Ts). The shaded areas in Fig. 12b,c are where absolute vorticity gradients cancel.

have shaded the areas where the flow reaches marginal stability, i.e. where absolute vorticity gradients cancel and potential vorticity develop a plateau. This clearly happens first only within the most intense part of the westward return flow.

It is necessary to wait until $t = 3.2\tau a$ to observe the first meanderings of the eastward jet (see Fig. 12c). This is clearly illustrated in Fig. 11b

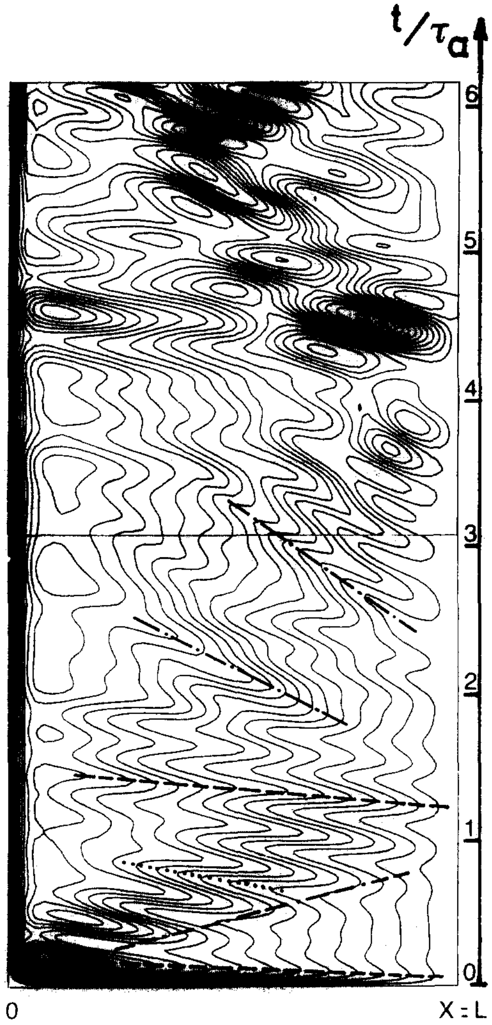

Fig. 13. Time history diagram of the streamfunction along the zonal section $y = 0.25L$ for experiment 11. (C.I. = 0.06 Ts). The different broken lines correspond to the propagation of: - - - - - -: long westward free Rossby waves, — — —: short eastward free Rossby waves, · · · · · ·: basin mode Rossby wave (1,2), · — · — ·: westward advection and propagation of barotropic instabilities.

corresponding to the time history of the streamfunction along the zonal section $y = 0.505L$, near the axis of the jet. We can see that these meanders are advected eastward but also propagate westward to destabilize most of the jet, as already noticed for experiment 27. In Fig. 12c, it must be noticed that the shaded areas, where potential vorticity gradients cancel and develop absolute vorticity plateaux, are now situated on the one hand within the return flows, as previously, and, on the other hand, on the two sides of the eastward jet. This is consistent with the conclusions of Talley (1983) on the radiating instability of the westward jets and the confined instability of the eastward ones.

This spin-up can also be followed in Fig. 13, which shows the evolution of the streamfunction along a $y = 0.25L$ zonal section: during the early stages of the spin-up, transport grows linearly until the fast Rossby wave generated at the eastern wall blocks this increase; simultaneously, a short Rossby wave front propagates eastward, leaving in its lee a wave pattern with a period exactly corresponding to that of the first basin Rossby mode (Anderson and Gill, 1975). It can be seen from this figure that the western boundary is nearly stabilized at $t = 1.5\tau a$, when the jet reaches the eastern boundary. The impact of the jet produces new westward fast Rossby waves that cross the basin and reinforce the western boundary current and the transport in the jet (see in Fig. 11b and 13, between $t = \tau a$ and $2\tau a$). Correlatively, instabilities appear on the two flanks of the return flow, and their advection can be followed in Fig. 13. These patterns can also be seen in the recirculating flows in Fig. 12b,c.

The destabilization of the jet, and its shortening then follows the same scenario as in experiment 27, with, however, much stronger transient Rossby waves generated from the extremity of the jet, and filling all the basin (Fig. 12d,e). This is because energy levels are now much higher. The same kind of spin-up and destabilization occur for experiments 4 and 23, corresponding to the same $\delta i/\delta f$ ratio, but higher and lower wind forcing, respectively.

This set of experiments leads us to draw a qualitative frontier between stable and unstable flows, in the (δi, δf) parameter space. For large δi, this frontier must follow the curve $\delta i/\delta f = 4$; for smaller δi, the domain of instability must be enlarged, in relation to the increase of transport observed in that area (see Fig. 7 and section 5.1).

5.3. Main characteristics of the unsteady cases

As pointed out in the preceding chapter, a 'statistically' steady state is reached for each unstable case after a spin-up phase of from 4 to $5\tau a$. From the observation of sequences of instantaneous streamfunction pictures like those displayed in Figs. 10d and 12f, it appears that the main features of this class of flows are:

(1) a barotropically unstable mid-latitude jet, meandering along the zero wind stress curl line, and producing occasional eddies resulting from cutting off these meanders;

(2) a westward drift of these eddies after their expulsions from the jet, the anticyclonic ones northwards, the cyclonic ones southwards; and

(3) a Rossby wave pattern filling all the basin with parabolic crests focussing on the extremity of the jet and propagating westward, just like free waves generated from a source point.

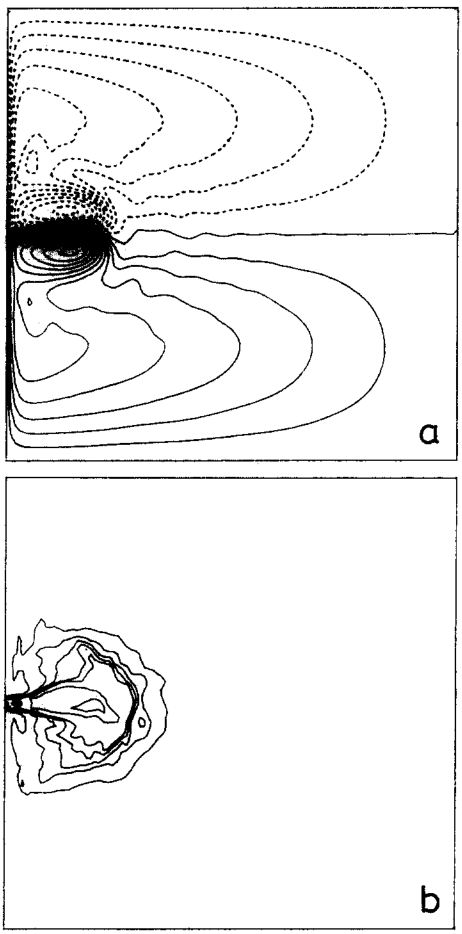

Fig. 14. Mean fields for experiment 27 calculated from an average of 300 instantaneous fields taken over a period of $4\tau a$. (a) mean streamfunction (C.I. = 0.16 Ts), (b) mean eddy kinetic energy distribution.

The mean transport pattern resulting from these flows is very different from those previously described in the steady state cases. One such example is presented in Fig. 14a, corresponding to experiment 27. A superposition of two scales of circulation is apparent: a large-scale Sverdrup circulation and a smaller recirculating gyre in each half basin. These inner gyres are embedded in the large-scale circulation pattern and look very similar to those discussed by Schmitz and Holland (1982) in the upper layer of a two layer stratified ocean.

The dynamics of these mean gyres has been analysed by Marshall (1984) in the context of barotropic instability only. Contrasting with the classical steady wind driven circulation cases, where an inertial-frictional boundary layer is needed to dissipate vorticity and allow the flow to return to the interior, equilibrium now also partly results from an internal redistribution of vorticity between the northern and southern gyres supplied by the eddies. The same was also discussed in Harrisson and Holland (1981) for a two layer ocean.

Maximum transport in each half basin is considerably increased compared with the steady state solutions; for example it is 1.7 Ts in experiment 27 and 1.86 Ts in experiment 23.

The eddy kinetic energy is concentrated in the vicinity of the jet, with a maximum at its eastern extremity where most of the eddies are produced; it falls off on the two flanks of the recirculating inner gyres (Fig. 14b). The mean to eddy kinetic energy ratios are highly dependent on the forcing and dissipation conditions. In Table II, strongly marked differences are noticeable between experiments that lie close together in parameter space (experiments 27 and 28): mean transport in the subgyres varies in relation with the KE′ level of course, while the eastward jet extension declines as a function of the degree of instability.

TABLE II

Mean to eddy kinetic energy ratio over the basin, eastward extension of the mean jet, and mean transport of the inner gyres

	Two very close experiments		A group of three experiments corresponding to the same forcing and bottom friction but increasing lateral dissipation		
	Experiment No.				
	28	27	23	24	25
KE'/KE	0.23	0.54	1.08	0.85	0.58
Lj/L	0.24	0.2	0.25	0.37	0.50
T/Ts	1.11	1.6	1.86	1.8	1.4

It would be interesting to investigate the relationship between these unsteady cases more carefully, particularly the rationalization of the jet's eastward penetration and its eddy kinetic energy for the statistically steady states with reference to forcing and dissipation parameters. But this is out of the scope of the present paper, which is limited to the transition from steady to unsteady cases.

6. ROLE OF LATERAL FRICTION

As observed in section 3, the biharmonic friction contribution cannot be ignored, especially with respect to the unstable cases, because the eddy sizes

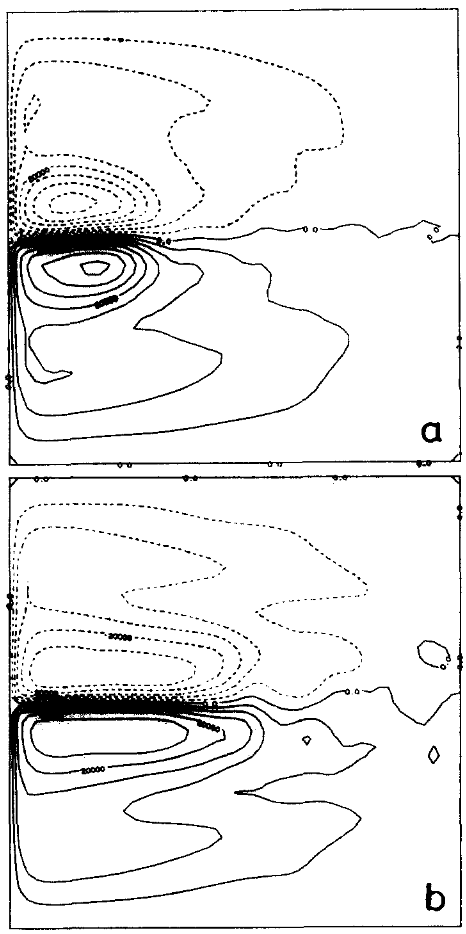

Fig. 15. Mean streamfunction fields for (a) experiment 23 and (b) experiment 25, calculated from an average of a sequence of instantaneous fields over $4\tau a$. (C.I. $= 0.265$ Ts).

are small enough to become highly sensitive to the enstrophy dissipation modelling.

Experiments 23, 24 and 25 illustrate how sensitive these unstable solutions are to the biharmonic friction coefficient, even in the context of slip boundary conditions. The forcing and bottom friction parameters are the same for the three experiments, but the A_4 coefficient is multiplied by 10 and 100, respectively, for experiments 24 and 25 as compared with experiment 23. The mean streamfunction patterns are displayed in Fig. 15 for experiment 23 and 25, while Table II contains the values of the mean to eddy kinetic energy ratios, the relative mean jet extension, and the relative mean transport for all these experiments. As expected, it can be seen that the increase of lateral friction is selectively acting at the smaller scales, reducing the tendency of the flow to develop instabilities and thus the mean transport in the sub-gyres. Correlatively, the flow inertias are increased and, consequently, so are the zonal penetration of the jet and the mean to eddy kinetic energy ratio. These results illustrate how substantially the preceding conclusions can be modified when larger values for lateral biharmonic friction are taken. This is even more the case when Laplacian friction is used (see, for example Böning (1986)).

7. CONCLUSION

The barotropic response of a square ocean driven by a steady double gyre antisymmetrical wind pattern was investigated by means of a large number of numerical experiments using a traditional range of external parameters (wind forcing and dissipation). Particular attention was paid to the major characteristics of the flow: eastward extension of the mid-latitude jet, width of the western boundary, width of jet and the maximum transport in the basin. Their dependence on the forcing and dissipation parameters (δi and δf) was examined, and rationalized, in the case of steady state solutions. A general dimensional relationship between Lj/L, T/Ts, δi and δf was established and validated by comparing it to experimental results. It shows the existence of different regimes for moderately or strongly non-linear flows. With the help of the experimental diagrams on Lj/L and T/Ts in the $(\delta i, \delta f)$ space, arising from this study, it is possible to quantitatively predict these quantities for given forcing and dissipation parameters.

The transition to barotropic instability was investigated in the controlling parameter space, by analysing the spin-up for certain experiments leading either to steady or unsteady solutions. Two different ways of destabilization were analysed, either by direct narrowing of the jet in relation with low forcing and dissipation, or by enhancement of the flow in the jet through the set up of strongly non-linear situations. Two types of destabilization were identified, namely through the generation and radiation of Rossby wave patterns on the two flanks of the westward return flows, and the meandering of the mid-latitude eastward jet.

The characteristics of the quasi steady flows, for the unstable solutions, are highly dependent on the external parameters: the eastward extension of the mean jet is closely related to its level of instability, and the same holds for mean transport in the inner gyres. A particular set of experiments was included in this context to show how sensitive the solutions are to lateral friction parameterization. By selectively acting on the small scales, with harmonic or biharmonic friction, the eddy kinetic energy level of the flow and transport in the inner gyres can be reduced, and the length of the mid-latitude jet is thus increased.

The dissipation ranges in the ocean are probably even lower than those used here. The present investigations thus need to be extended to very small δf. But it must be pointed out that these results are probably also very dependent on the strict antisymmetry of the wind forcing pattern used. Harrison and Stalos (1982) have provided some illustrations of major changes in the dynamical response of flows driven by significantly different wind forcing. This will be investigated in a future study, in relation to an analysis of the influence of time and space variabilities in forcing on the general oceanic circulation.

ACKNOWLEDGEMENTS

This work has been supported by CNRS and IFREMER through the Programme National d'Etude de la Dynamique du Climat. The calculations have been made with the numerical facilities of the Centre de Calcul Vectoriel pour la Recherche in Palaiseau. The authors are indebted to the referees for helpful comments and suggestions.

REFERENCES

Anderson, D. and Gill, A., 1975. Spin-up of a stratified ocean with applications to upwelling. Deep-Sea Res., 24: 709–732.

Azakawa, A., 1966. Computational design for long term integration of the equations of fluid motions. J. Comp. Phys., 1: 119–143.

Blandford, R.R., 1971. Boundary conditions in homogeneous ocean models. Deep-Sea Res., 18: 739–751.

Böning, C.W., 1986. On the influence of frictional parametrization in wind-driven ocean circulation models. Dyn. Atmos. Oceans, 10: 63–92.

Bryan, K., 1963. A numerical investigation of a non-linear model of a wind-driven ocean. J. Atmos. Sci., 20: 549–606.

Carrier, G.F. and Robinson, A.R., 1962. On the theory of the wind-driven ocean circulation. J. Fluid Mech., 12: 49–80.

Charney, J.G., 1955. The Gulf Stream as an inertial boundary layer. Proc. Natl. Acad. Sci., 41: 731–740.

Charney, J.G., 1971. Geostrophic turbulence. J. Atmos. Sci., 28: 1087–1097.

Fofonoff, N.P., 1954. Steady flow in a frictionless homogeneous ocean. J. Mar. Res., 13: 254–262.

Harrison, D.E., 1982. On deep mean flow generation mechanisms and the abyssal, circulation of numerical model gyres. Dyn. Atmos. Oceans, 6: 135–152.

Harrison, D.E. and Holland, W.R., 1981. Regional eddy vorticity transport and the equilibrium vorticity budgets of a numerical model ocean circulation. J. Phys. Oceanogr., 11: 190–208.

Harrison, D.E. and Stalos, S., 1982. On the wind driven ocean circulation. J. Mar. Res., 40: 773–791.

Holland, W.H., 1967. On the wind driven circulation in an ocean with bottom topography. Tellus, 19: 582–599.

Holland, W.H., 1978. The role of mesoscale eddies in the general circulation of the ocean. Numerical experiments using a wind driven quasi-geostrophic model. J. Phys. Oceanogr., 8: 363–392.

Marshall, J.C., 1984. Eddy-mean flow interaction in a barotropic ocean model. Q. J. R. Meteorol. Soc., 110: 465: 573–590.

Moore, D.W., 1963. Rossby waves in ocean circulation. Deep Sea Res., 25: 859–910.

Morgan, G.W., 1956. On the wind driven ocean circulation. Tellus, 8: 301–320.

Munk, W.H., 1950. On the wind driven ocean circulation. J. Meteorol., 7: 79–93.

Niiler, P.P., 1966. On the theory of the wind driven ocean circulation. Deep-Sea Res., 13: 597–606.

Pedlosky, J., 1979. Geophysical Fluid Dynamics. Springer-Verlag, Berlin, 286 pp.

Schmitz, W.J. and Holland, W.H., 1982. Numerical eddy resolving general circulation experiments: preliminary comparison with observations. J. Mar. Res., 40, 1: 15, 117.

Stewart, R.W., 1964. The influence of friction an inertial models of oceanic circulation. Stud. Oceanogr., 3–9.

Stommel, H., 1948. The westward intensification of wind driven ocean currents. Trans. Am. Geophys. Union, 29: 202–206.

Sverdrup, H.U., 1947. Wind driven currents in a barotropic ocean: with application to the equatorial currents of the Eastern Pacific. Proc. Nat. Acad. Sci., 33: 318–326.

Talley, L.D., 1983. Radiating barotropic instability. J. Phys. Oceanogr., 13: 972–987.

Veronis, G., 1964. On inertially controlled flow patterns in a β-plane ocean. Tellus, 15: 59–66.

Veronis, G., 1966a. Wind driven ocean circulation. Part 1: Linear theory and perturbation analysis. Deep Sea Res., 13: 17–29.

Veronis, G., 1966b. Wind driven ocean circulation. Part 2: Numerical solution of the non-linear problem. Deep-Sea Res., 13: 31–55.